Oxidative Addition of Dihydrogen to [Ir(bisphosphine)(1,5-cyclooctadiene)]BF_4 Complexes: Kinetic and Thermodynamic Selectivity

Barbara F. M. Kimmich, Ekasith Somsook, and Clark R. Landis*

Contribution from the Department of Chemistry, University of Wisconsin−Madison, 1101 University Avenue, Madison, Wisconsin 53706

Received May 4, 1998

Abstract: The activation of dihydrogen by cationic diphosphine complexes of Rh is the rate-determining and enantiodetermining step in the catalytic asymmetric hydrogenation of prochiral enamides. The addition of H_2 to [Ir(bisphosphine)(COD)]$^+$ (COD = 1,5-cyclooctadiene) complexes is examined herein as a model for stereocontrol and dynamic processes related to catalytic hydrogenation. The diastereoselectivity of H_2 oxidative addition to form diastereomeric [Ir(chiral bisphosphine)$(H)_2$(COD)]$^+$ complexes at −80 °C is kinetically controlled and varies substantially with the structure of the diphosphine. In one instance (chiral bisphosphine = CHIRAPHOS), the kinetic and thermodynamic selectivities of H_2 addition are inverted; i.e., the dominant kinetic product is thermodynamically less stable than the minor kinetic product. For the [IrH_2(Me-DuPhos)-(COD)]$^+$ system, quantitative analysis of the 2D NOE data using two-dimensional conformer population analysis (2DCPA) establishes the absolute stereochemistry and the three-dimensional structures of the predominant conformers. Kinetic analysis of the interconversion of the [IrH_2(Me-DuPhos)(COD)]$^+$ diastereomers, and of their exchange with D_2, reveals a complex pathway for isotope scrambling and diastereomer interconversion that does not involve reductive elimination of H_2 to form [Ir(Me-DuPhos)(COD)]$^+$. During the isotope scrambling, exquisite selectivity is seen for exchange in only two ligand sites, one on the Me-DuPHOS ligand and one on the COD ligand.

Introduction

The catalytic asymmetric hydrogenation of prochiral substrates continues to be an active area of industrial and academic research. For example, Novartis recently announced a commerical process for the catalytic asymmetric hydrogenation of imines using homogeneous iridium catalysts.[1] The first successful catalytic asymmetric hydrogenation reactions involved the reduction of prochiral enamides.[2−4] Other notable recent developments primarily involve the synthesis of new rigid diphosphine ligands that exhibit high enantiospecificity over a broad range of enamide and related substrates.[2,4]

A critical step in hydrogenation reactions catalyzed by transition metal complexes is the activation of dihydrogen. For example, although the phenomenological steps of catalytic enamide hydrogenation are well understood,[5−7] good models of the turnover-limiting and enantiodetermining transition states have not yet emerged. Most current interpretations[5−7] invoke a hydrogen activation that proceeds via H_2 oxidative addition followed by insertion of the alkene into a M−H bond. The recent characterization of a dihydride intermediate by Bargon and co-workers[8] via *para*-H_2 enhanced ^{1}H NMR spectroscopy has provided the first direct evidence for the existence of such dihydrides under catalytic hydrogenation conditions. Whether these complexes are intermediates or the products of side equilibria in the catalytic cycle currently is unknown.

In contrast with the olefinic rhodium complexes of cis-chelating diphosphines, dihydrides of analogous iridium complexes can be observed directly by NMR spectroscopy. As a result, stable dihydrides are readily observed for iridium complexes of cyclooctadiene at −80 °C.[9] This provides the opportunity to explore factors influencing the selectivity of authentic oxidative addition reactions and their subsequent rearrangement dynamics.[10] Although iridium complexes may exhibit different catalytic activities and mechanisms than analogous rhodium complexes, we note that diastereomeric enamide complexes of the two metals with chiral diphosphines exhibit similar stereoselectivities upon reaction with H_2, with the more stable diasteromer being less reactive toward H_2.[11] These results suggest that stereodifferentiating interactions in the transition states for dihydrogen activation by rhodium complexes may be modeled well by the corresponding iridium complexes.

This paper contains a detailed description of the oxidative addition of dihydrogen to a series of [Ir(bisphosphine)(COD)]-BF_4 complexes (COD = 1,5-cyclooctadiene). First, we present data on the intrinsic diastereoselectivity of the oxidative addition

(1) Blaser, H. U.; Spindler, F. *Top. Catal.* **1997**, *4*, 275−282.
(2) *Applied Homogeneous Catalysis with Organometallic Compounds*; Cornils, B., Herrmann, W. A., Eds.; VCH: Weinheim, 1996.
(3) Ojima, L.; Clos, N.; Bastos, C. *Tetrahedron* **1989**, *45*, 6901.
(4) *Catalytic Asymmetric Synthesis*; Ojima, I., Ed.; VCH Publishers: New York, 1993.
(5) Landis, C. R.; Halpern, J. *J. Am. Chem. Soc.* **1987**, *109*, 1746.
(6) Brown, J. M.; Chaloner, P. A.; Morris, G. A. *J. Chem. Soc., Perkins Trans. 2* **1987**, 1583.
(7) Brown, J. M.; Chaloner, P. A.; Morris, G. A. *J. Chem. Soc., Chem. Commun.* **1983**, 664.
(8) Harthun, A.; Kadyrov, R.; Selke, R.; Bargon, J. *Angew. Chem., Int. Ed. Engl.* **1997**, *36*, 1103.
(9) Crabtree, R. H.; Felkin, H.; Morris, G. E. *J. Chem. Soc., Chem. Commun.* **1976**, 716.
(10) Brauch, T. W.; Landis, C. R. *Inorg. Chim. Acta* **1998**, *270*, 285−297.
(11) Armstrong, S. K.; Brown, J. M.; Burk, M. J. *Tetrahedron Lett.* **1993**, *34*, 879−882.

S0002-7863(98)01536-4 CCC: $15.00
Published on Web 09/22/1998

Table 1. ^{1}H and ^{31}P NMR Spectral Data for $[IrH_2(P-P)(COD)]BF_4$ in CD_2Cl_2 at −80 °C

$[IrH_2(COD)(P-P)]BF_4$ isomer, P−P =		^{1}H NMR[a] hydride region, δ (ppm)		^{31}P NMR[b] {^{1}H},[b] δ (ppm)	
		IrH_{cis} (J_{P-H}, Hz)	IrH_{trans} (J_{P-H}, Hz)	P_{trans} (J_{P-P}, Hz)	P_{cis} (J_{P-P}, Hz)
6, (*S*,*S*)-DIOP[c]	maj (a)	−14.18, dd (24, 16)	−9.70, dd (90, 10)	25.2 br s	−7.2 br s
	min (b)	−15.25, t (15)	−8.9, dd (92, 14)	−31.6 br s	−8.9 br s
7, (*S*,*S*)-CHIRAPHOS[c]	maj (b)	−13.45, t (16)	−9.89, dd (74, 12)	28.2 d (12)	32.5 d (12)
	min (a)	−12.73, t (15)	−10.48, dd (88, 12)	29.5 d (15)	38.4 d (18)
8, (*R*)-BINAP[c]	(b)	−13.41, dd (28, 11)	−11.81, dd (88, 10)	−19.8 br d (18)	13.9 d (18)
9, (*R*)-Tol-BINAP[c]	(b)	−13.25, dd (23, 12)	−11.70, dd (94, 11)	−21.3 br d (18)	11.8 d (21)
10, (*R*,*R*)-Me-DuPHOS	maj (a)	−15.66, dd (23, 17)	−10.38, dd (88, 16)	22.1 br d (12)	54.4 d (9)
	min (b)	−14.04, t (21)	−9.85, dd (110, 19)	38.1 br d (12)	40.1 d (9)
14, (*R*,*R*)-NORPHOS[c]	(a)	−12.42, dd (20, 14)	−11.08, dd (92, 19)	−8.2 br s	10.3 d (18)
	(c)	−13.54, dd (24, 12)	−11.70, dd (96, 16)	−16.5 br s	8.2 d (18)
	(d)	−14.00, dd (20, 13)	−10.13, dd (90, 17)	−5.6 br s	−7.7 d(18)
	(b)	−13.12, t (16)	−10.46, dd (92, 17)	−4.9 br s	1.2 d (18)
15, (*S*,*R*)-BPPFA[d]	i	−12.96, dd (26, 18)	−11.36, dd (93, 32)	−5.6 d (18)	1.6 d (18)
	ii	−13.29, t (21)	−10.03, dd (91, 28)	−10.6 d (18)	1.4 d (15)
	iii	−12.81, dd (32, 16)	−11.4, m overlap	−19.4 d (18)	4.3 d (18)
	iv	−12.9, m overlap	−10.89 dd (98, 26)	−17.47 br s	2.8 br s
16, (*S*,*R*)-BPPFAc[d]	maj	−12.73, dd (31, 16)	−11.22 dd (96, 31)	−18.8 d (20)	4.1 d (20)
	min	−13.96, dd (28, 17)	−11.82 dd (96, 28)	−6.3 d (20)	1.9 d (20)

[a] 500 MHz. [b] 202 MHz. [c] Isomer designation based on literature assignments for $[IrH_2(bisphosphine)(COD)](CF_3SO_3)$ at −30 °C.[9,15,16] [d] The absolute configurations of the metal centers were not determined; the ordering of isomers corresponds to the ordering of the ratios presented in Table 2.

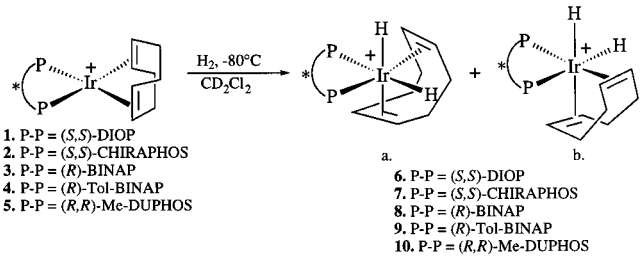

Figure 1. Oxidative addition of H_2 to $[Ir(bisphosphine)(COD)]^+$ complexes containing C_2-symmetric bisphosphines.

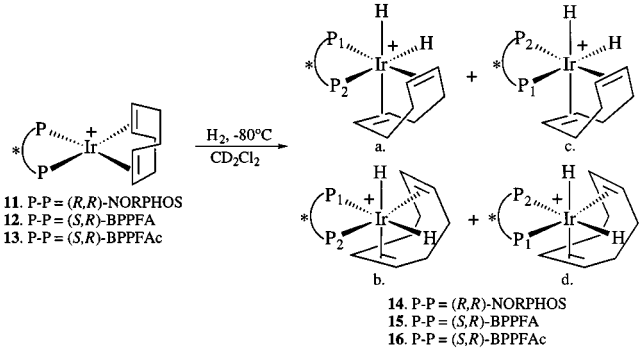

Figure 2. Oxidative addition of H_2 to $[Ir(bisphosphine)(COD)]^+$, where the bisphosphine is C_1-symmetric.

of hydrogen to a series of $[Ir(bisphosphine)(COD)]BF_4$ complexes containing chiral C_2- and C_1-symmetric bisphosphines (Figures 1 and 2). This is followed by an in-depth study of the oxidative addition of H_2 to $[Ir(R,R)$-Me-DuPHOS$)(COD)]BF_4$. Included are the determination of the solution structure and absolute configuration of the major dihydride and the determination of the mechanisms of diastereomer and isotopic label exchange.

Results and Discussion

Formation of IrH_2(bisphosphine)(COD)]BF_4 Complexes. Complexes of the type $[Ir(phosphine)_2(COD)]^+$ have been known for several decades.[12−14] These highly colored species previously have been observed to react with dihydrogen at low temperatures to give colorless or pale colored $[IrH_2(phosphine)_2(COD)]^+$ complexes.[9,15,16] When $[Ir(bisphosphine)(COD)]^+$ complexes containing C_2-symmetric chiral bisphosphines such as (*S*,*S*)-CHIRAPHOS, (*S*,*S*)-DIOP, (*R*)-BINAP, (*R*)-Tol-BINAP, or (*R*,*R*)-Me-DuPHOS are reacted at −80 °C with dihydrogen, two diastereomeric dihydrides can be formed (Figure 1). The iridium dihydrides exhibit a characteristic P−H coupling pattern in the hydride region of the ^{1}H NMR (Table 1). As shown in Table 2, the diastereomer ratios depend on the diphosphine used and the reaction temperatures.

The $[Ir(bisphosphine)(COD)]BF_4$ complexes of C_1-symmetric ligands such as (*R*,*R*)-NORPHOS, (*S*,*R*)-BPPFA, or (*S*,*R*)-BPPFAc react to yield up to four dihydrides (Figure 2). For example, $[IrH_2((S,R)$-BPPFA$)(COD)]BF_4$ (**15**) forms as a mixture of four isomers in an approximate ratio of 25:18:28:1 (Tables 1 and 2). Previously, Hälg and Rüegger[15,16] reported similar NMR results for some of the diphosphines listed here (Tables 1 and 2). The absolute configurations given in Table 2, except for the Me-DuPHOS ligand, are based on the assignments of Hälg *et al.*[15,16]

Kinetic vs Thermodynamic Control of the Oxidative Addition Reactions. Oxidative addition selectivity varies with temperature. To probe whether the selectivity was under thermodynamic or kinetic control, a series of warming experiments was performed. In a typical experiment, the dihydride was prepared at −80 °C and then warmed in a −45 °C bath, and NMR spectra were taken at −80 °C (Figure 3). The dihydride product ratios did not change substantially when the samples were stored at −80 °C. Results of the warming experiments are given in Table 2. For example, when $[IrH_2$-(Me-DuPHOS)(COD)]BF_4 was warmed at −45 °C, the initial 47:1.0 ratio of diastereomers was found to equilibrate to 5.8:1.0 (Table 2 and Figure 3). The equilibration occurred without any noticeable decomposition of the dihydride complexes.

Oxidative additions of hydrogen to $[Ir((S,S)$-CHIRAPHOS$)$-$(COD)]BF_4$ and $[Ir((R,R)$-NORPHOS$)(COD)]BF_4$ (Table 2) are

(12) Schrock, R. R.; Osborn, J. A. *J. Am. Chem. Soc.* **1971**, *93*, 3089.
(13) Haines, L. M.; Singleton, E. *J. Chem. Soc., Dalton Trans.* **1972**, 1891.
(14) Hälg, W. J.; Öhrström, L. R.; Rüegger, H.; Venanzi, L. M. *Helv. Chim. Acta* **1993**, *76*, 788.
(15) Hälg, W. J.; Öhrström, L. R.; Rüegger, H.; Venanzi, L. M. *Magn. Reson. Chem.* **1993**, *31*, 677.
(16) Hälg, W. J. Ph.D. Dissertation, ETH-Zürich, 1994.

Table 2. Selectivity of Oxidative Addition of H_2 to [Ir(bisphosphine)(COD)]BF_4

complex	$[IrH_2(P-P)(COD)]BF_4$, P−P =	kinetic ratio at −80 °C[a] (configuration at Ir)	thermodynamic ratio after equiliibration at −45 °C (configuration at Ir)	Hälg product ratio at −30 °C[f] (configuration at Ir)	twist distortion of square planar diene complex
6	(*S*,*S*)-DIOP	27:1.0	ca. 18:1[d]	13:1 (Λ)	
7	(*S*,*S*)-CHIRAPHOS	1.0:1.8	6.1:1.0	5:1 (Λ)	+9.2[g]
8	(*R*)-BINAP	>50:1	ca. >50:1.0[e]	99:1 (Δ)	−14.9[h]
9	(*R*)-Tol-BINAP	>50:1	ca. >50:1.0[e]		
10	(*R*,*R*)-Me-DuPHOS	47:1.0 (Λ, OC-6-23)	5.8:1.0 (Λ)		+15.6
14	(*R*,*R*)-NORPHOS[c]	26:23:3:1	15:6:1.0:1.2	7:1 (Δ)	−4.0[i]
15	(*S*,*R*)-BPPFA[c]	25:18:28:1[b]	ca. 7.1:1.6:1.0:1.0[d]		
16	(*S*,*R*)-BPPFAc[c]	1.3:1.0	ca. 1:19[d]		

[a] Ratio determined by ^{1}H NMR spectra taken at −80 °C unless otherwise indicated. [b] Ratio determined by ^{31}P NMR spectra taken at −80 °C due to overlap in the ^{1}H NMR. [c] C_1-symmetric diphosphines yield four dihydride isomers. [d] Dihydride ratio changes, but decomposition occurs; thermodynamic equilibrium is estimated. [e] Decomposition of the major dihydride occurs, and a second dihydride isomer cannot be characterized; thermodynamic equilibrium is estimated. [f] Results as determined by Hälg and co-workers.[15,16] [g] Cambridge refcode: OCPBRH. [h] Cambridge refcode: BNAPRH10. [i] Cambridge refcode: HATJOB.

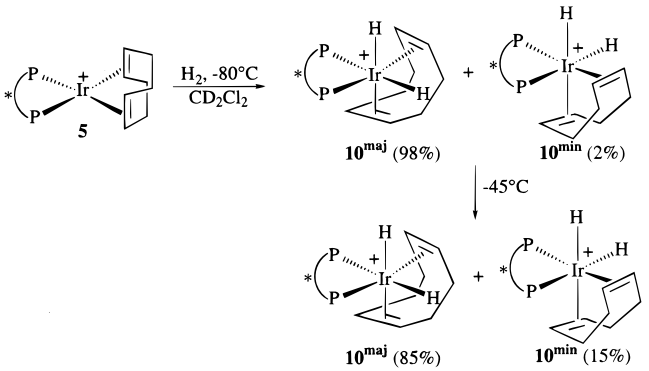

Figure 3. Warming experiment for $[IrH_2(Me\text{-}DuPHOS)(COD)]BF_4$.

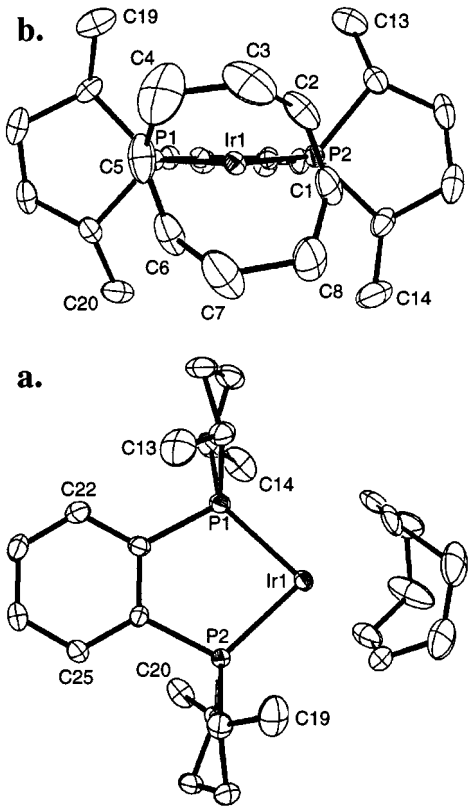

Figure 4. Crystal structure of [Ir((*R*,*R*)-Me-DuPHOS)(COD)]BF_4 (**5**). (a) Top view and (b) side view showing the planarity of the phenylene unit. Hydrogens and BF_4^- counterion were omitted for clarity.

also under kinetic control. On warming of a solution of $[IrH_2$-((*R*,*R*)-NORPHOS)(COD)]BF_4 (**13**) to −45 °C, the initial kinetic ratio of 26:23:3:1 gave a thermodynamic ratio of 15:6:1.0:1.2. The CHIRAPHOS analogue displayed an even greater differentiation between kinetic and thermodynamic control. The kinetically favored CHIRAPHOS diastereomer $\mathbf{7}^{maj}$ (product ratio 1.8:1.0) was found to be the thermodynamically disfavored product (1:6.1 ratio) at −45 °C. Under similar conditions, Hälg[16] reports substantial decomposition of $[IrH_2((S,S)$-CHIRAPHOS)(COD)]$^+$; the origin of this discrepancy with our results is unclear.

The remaining dihydrides (**6**, **8**, **9**, **15**, and **16**) decompose to varying degrees on warming to −45 °C. The BINAP-based dihydrides **8** and **9** decomposed slowly to give complex mixtures which could not be fully characterized. The DIOP analogue decomposed somewhat more rapidly, yielding a single species containing one hydride resonance, which has not been fully characterized. The decomposition of the dihydride is accompanied by a moderate decrease of the product ratio from 27:1 to 18:1. Similarly, the $[IrH_2(BPPFA)(COD)]BF_4$ **15** reacted to give a single apparent monohydride in solution, accompanied by a variation of the dihydride ratio (product ratio decreased from 25:18:28:1 to 7.1:1.6:1.0:1.0). Because of the decomposition reactions at −45 °C, we are only able to estimate the thermodynamic selectivities.

At −80 °C, the oxidative additions of H_2 to [Ir(bisphosphine)-(COD)]BF_4 appear to be under kinetic control. This result is in agreement with Eisenberg's studies of the related dihydride systems IrBr(CO)(CHIRAPHOS) and IrX(CO)(DIPHOS) (X = Cl, Br, I, CN, PPh_3, H).[17−20] Since the reactions are under kinetic control, molecular modeling calculations, which are based on the stabilities of the dihydride compounds and their intermediates, will not necessarily model the reaction selectivity.[21]

Crystallographic Structure of [Ir((*R*,*R*)-Me-DuPHOS)-(COD)]BF_4. [Ir(Me-DuPHOS)(COD)]BF_4 (**5**) was isolated as dark brown needles from CH_2Cl_2/Et_2O. The crystal structure of **5** is shown in Figure 4, and relevant bond distances and angles are given in Table 3. This structure, which is very similar to that of [Rh(COD)((*S*,*S*)-Me-DuPHOS)]SbF_6,[22] provides important information about the asymmetric environment at the Ir

(17) Kunin, A. J.; Farid, R.; Johnson, C. E.; Eisenberg, R. *J. Am. Chem. Soc.* **1985**, *107*, 5315.
(18) Johnson, C. E.; Fisher, B. F.; Eisenberg, R. *J. Am. Chem. Soc.* **1983**, *105*, 7772.
(19) Johnson, C. E.; Eisenberg, R. *J. Am. Chem. Soc.* **1985**, *107*, 3148.
(20) Deutsch, P. P.; Eisenberg, R. *Chem. Rev.* **1988**, *88*, 1147.
(21) Giovannetti, J. S.; Kelly, C. M.; Landis, C. R. *J. Am. Chem. Soc.* **1993**, *115*, 4040−4057.
(22) Burk, M. J.; Feaster, J. E.; Nugent, W. A.; Harlow, R. L. *J. Am. Chem. Soc.* **1993**, *115*, 10125.

Table 3. Selected Interatomic Distances and Intramolecular Angles for [Ir((*R*,*R*)-Me-DuPHOS)(COD)]BF_4

Interatomic Distances (Å)			
Ir(1)−P(1)	2.2839(8)	Ir(1)−C(5)	2.214(4)
Ir(1)−P(2)	2.2796(8)	Ir(1)−C(6)	2.188(4)
Ir(1)−C(1)	2.233(3)	C(1)−C(2)	1.373(6)
Ir(1)−C(2)	2.197(3)	C(5)−C(6)	1.377(7)
Intramolecular Nonbonding Distances (Å)			
C(1)−C(14)	3.539	C(20)−C(25)	3.497
C(5)−C(19)	3.589	C(4)−C(8)	3.658
C(13)−C(22)	3.151		
Intramolecular Angles (deg)			
P(1)−Ir(1)−P(2)	85.33(3)	C(2)−Ir(1)−C(5)	80.0(1)
C(1)−Ir(1)−C(5)	93.3(2)	C(2)−Ir(1)−C(6)	89.1(2)
C(1)−Ir(1)−C(6)	80.1(2)	Ir(1)−P(2)−C(26)	109.7(1)

atom. Both the Ir−P bond lengths and the P−Ir−P bond angle (85°) are similar to those of the related [Ir(COD)((−)-NORPHOS)]PF_6 species.[15] As in [Rh(COD)((*S*,*S*)-Me-DuPHOS)]-SbF_6, the 1,2-phenylene ring unit is essentially planar, and only a 6.3° dihedral twist out of the P−Ir−P plane is observed. The rigidity of this unit positions the phospholane methyl groups close to the Ir coordination sphere, allowing for efficient stereochemical communication. The large dihedral angle of 15.6° observed between the P−Ir−P plane and the plane defined by the COD olefin midpoints is again similar to the 18° dihedral angle seen in the rhodium analogue.

Correlation of Oxidative Addition Selectivity with the Crystallographic Structures of [Ir(bisphosphine)(diolefin)]$^+$ Complexes. In previous investigations of the enamide hydrogenation using complexes of the Me-DuPHOS ligand, Brown and Burk[11] noted an interesting correlation of the direction of torsional twist between planes defined by P−Rh−P and centroid$_{C=C}$−Rh−centroid$_{C=C}$ positions with the sense of chirality in enamide hydrogenation. Using the definition of "twist angle" diagrammed below, we have examined the correlation

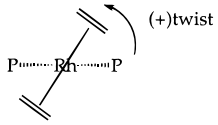

between the magnitude and sign of the twist angle with the sign and extent of diastereoselectivity in the oxidative addition of dihydrogen (see Table 2, columns 3 and 6) to a variety of [Ir(bisphosphine)(COD)]$^+$ complexes. For the DuPHOS, NORPHOS, and BINAP ligands, the kinetically preferred dihydride diastereomer correlates with the sign of twist angle according to (+)twist↔Λ and (−)twist↔Δ. However, for CHIRAPHOS, the kinetically preferred dihydride diastereomer slightly prefers the Δ configuration at the metal but has a (+)twist. In all four cases, the sense of the thermodynamically preferred configuration in the dihydride correlates with the sense of the twist angle in the solid-state structure of the [Ir(bisphosphine)(COD)]$^+$ complex.

Correlation of Oxidative Addition Selectivity with Enamide Catalytic Hydrogenation Selectivity. Because the sense of diene twist angle correlates with the sense of product chirality in enamide hydrogenation,[11] as discussed above, we were also interested to see if the sense and magnitude of kinetically controlled diastereoselective H_2 addition to [Ir(bisphosphine)-(COD)]$^+$ complexes correlates with enamide enantioselectivity. The selectivity of oxidative addition of H_2 to [Ir(bisphosphine)-(COD)]BF_4 (Table 2) partially correlates to the selectivity of the hydrogenation of prochiral enamides (Table 4). High selectivities are observed in both oxidative addition and enamide hydrogenation for BINAP, Tol-BINAP, and Me-DuPHOS complexes. In contrast, the CHIRAPHOS-based complex **2** exhibits poor selectivity in oxidative addition of dihydrogen (diastereomeric product ratio 1.8:1.0) but significant selectivity as an enamide hydrogenation catalyst (enantiomeric product ratio = 10.1:1).

Table 4. Comparison of the Selectivity of the [Rh(P−P)(NBD)]$^+$-Catalyzed Hydrogenation of Prochiral Enamides with the Kinetic Selectivity of H_2 Addition to [Ir(P−P)(COD)]$^+$ Complexes

ligand (P−P) and kinetic selectivity of H_2 addition to [Ir(P−P)(COD)]$^+$	substrate[a]	enatiomeric ratio of the product	ref
(*S*,*S*)-CHIRAPHOS, 1.8:1 (Λ) +	R = Me; R′ = Pr	10.1:1 (*R*:*S*)	23
	R = Me; R′ = H	8.5:1	24
	R = Me; R′ = ^{i}Pr	5.6:1	23
(*S*,*S*)-DIOP, 27:1 (Λ)	R = Me; R′ = Ph	5.4:1 (*S*:*R*)	25
	R = Me; R′ = H	4.0:1	26
(*R*)-BINAP, >50:1 (Δ) −	R = Ph; R′ = Ph	99:1 (*S*:*R*)	27
(*R*,*R*)-Me-DuPHOS, 47:1 (Λ) +	R = Me; R′= H	199:1 (*R*:*S*)	22
(*R*,*R*)-NORPHOS, 26:23:3:1 (Δ) −	R = Me; R′ = Pr	8.5:1 (*S*:*R*)	23
(*S*,*R*)-BPPFA, 25:18:28:1	R = Me, R′ = Ph	1.5:1 (*S*:*R*)	24
(*S*,*R*)-BPPFAc, 1.3:1	R = Me, R′ = Ph	1.2:1 (*S*:*R*)	28

[a] 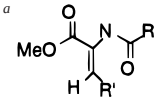

Stereochemistry of [IrH_2(Me-DuPHOS)(COD)]BF_4 (10^{maj}). The absolute configuration of the major diastereomer of [IrH_2-((*R*,*R*)-Me-DuPHOS)(COD)]BF_4 (**10^{maj}**) was determined using a combination of ^{1}H−^{1}H DQF COSY and ^{1}H−^{1}H NOESY 2D NMR experiments. The structure of **10^{maj}** is shown in Figure 5, and full ^{1}H assignments are given in Table 5 (^{31}P NMR data are given in Table 1). In addition to the COSY data, the configuration of the dihydride could be assigned on the basis of a number of important NOE interactions, in particular, those between protons H17−H28, H20−H16, H8−H1, H24−H4, H23−H18, H27−25A, H27−26A, H27−H19, and H27−H5 (Figure 5). These NOE interactions include those between the hydrides and methyl H's as well as NOEs between the methyl or methine H's and the phenylene moiety. The analysis of the 2D-NMR data allowed for the assignment of almost all of the individual protons of **10^{maj}** (34 total inequivalent protons). The methylene protons on the phospholane rings were the most difficult to assign, and, in several cases, the shifts of the two protons on a single carbon were essentially identical. While these protons could not be assigned for the complex in CD_2Cl_2, full assignments could be made for **10^{maj}** in acetone-d_6 (see Supporting Information). In the process of analysis, a number of long-range couplings between H24−H27 and H25B−H27 were found (see Figure 5). Similar long-range couplings were observed for [IrH_2((*R*,*R*)-NORPHOS)(COD)]CF_3SO_3 and [IrH_2-((*S*,*S*)-CHIRAPHOS)(COD)]CF_3SO_3, and these were attributed to (homo)allylic coupling pathways in which the metal orbitals play a mediating role.[15]

(23) Scott, J. W.; Keith, D. D.; Nix, C.; Parish, D. R.; Remington, S.; Roth, G. P.; Townsend, J. M.; Vanlentine, D.; Yang, R. *J. Org. Chem.* **1981**, *46*, 5086.
(24) Hayashi, T.; Mise, T.; Mitachi, S.; Yamamoto, K.; Kumada, M. *Tetrahedron Lett.* **1976**, 1133.
(25) Glaser, R.; Vainas, B. *J. Organomet. Chem.* **1976**, *121*, 249.
(26) Brown, J. M.; Murrer, B. A. *Tetrahedron Lett.* **1980**, 581.
(27) Miyashita, A.; Yasuda, A.; Takaya, H.; Toriymi, K.; Ito, T.; Souchi, T.; Nayora, R. *J. Am. Chem. Soc.* **1980**, *102*, 7932.
(28) Kimmich, B. F. M.; Landis, C. R. *Organometallics* **1996**, *15*, 4141.

Table 5. ^{1}H and ^{13}C Data for the Major Diastereomer of [IrH_2((*R*,*R*)-MeDuPHOS)(COD)]BF_4 (**10^{maj}**) in CD_2Cl_2 at −80 °C

C no.	δ(^{13}C)	J_{C-P} (Hz)	H no.[a]	J_{P-H} (Hz)	δ(^{1}H)	assignment
17	11.5		17		0.67	Me
6	14.4		6		0.33	Me
18	16.2		18		1.41	Me
5	21.9		5		1.26	Me
22	26.0		22B		2.22	COD CH_2
			22A		1.56	COD CH_2
26	27.3		26B		1.62	COD CH_2
			26A		2.52	COD CH_2
	34.3		4		2.02	*CH*CH_3(6)
	34.3−34.7[b]		15A/B		2.35	Me-DuPHOS CH_2
			2A/B		2.33	Me-DuPHOS CH_2
			3A/B		2.12	Me-DuPHOS CH_2
			15A/B		1.98	Me-DuPHOS CH_2
			3A/B		1.52	Me-DuPHOS CH_2
			2A/B		1.46	Me-DuPHOS CH_2
1	35.7	41	1		2.73	*CH*CH_3(5)
14	36.6		14A/B		1.82	Me-DuPHOS CH_2
			14A/B		2.44	Me-DuPHOS CH_2
25	37.9		25A		2.81	COD CH_2
			25B		3.39	COD CH_2
21	38.8		21B		2.50	COD CH_2
			21A		3.55	COD CH_2
16	39.5	34	16		2.68	*CH*CH_3(17)
13	44.9	20	13		3.03	*CH*CH_3(18)
23	72.7		23		4.67	COD vinyl
20	79.2		20		4.07	COD vinyl
19	82.2		19		4.90	COD vinyl
24	84.5		24		4.30	COD vinyl
8	130.4[c]		8		7.63	phenyl
9	130.4[c]		9		7.55	phenyl
10	131.3		10		7.59	phenyl
11	132.3	14	11		7.83	phenyl
7/12	140.1	49, 31				ipso
7/12	143.3	44, 29				ipso
			27	88, 16	−10.48[d]	IrH trans
			28	23, 17	−15.74[d]	IrH cis

[a] Differentiation of H's (A/B) on a single C for the phospholane CH_2 groups was not possible in CD_2Cl_2. [b] Peaks are not resolved in the carbon dimension of the HMQC. [c] Assignment of the ipso carbons is ambiguous. [d] The ^{1}H NMR shifts above were derived from the DQF COSY. These differ slightly from those derived from the 1D ^{1}H NMR.

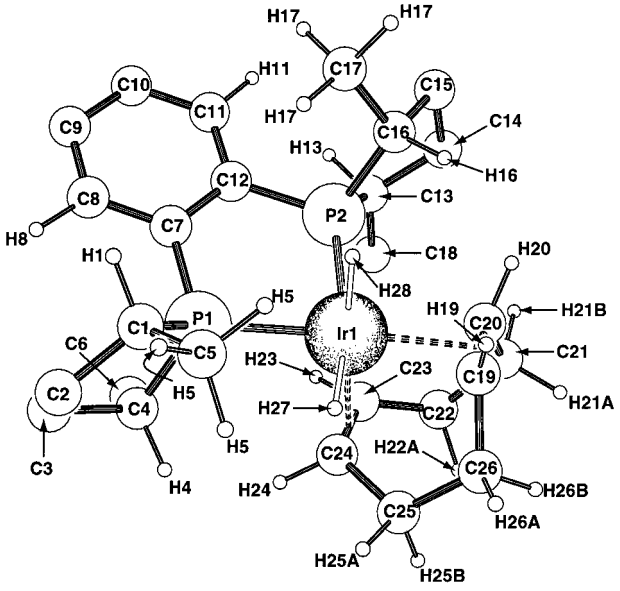

Figure 5. Dominant solution conformation of [IrH_2(Me-DuPHOS)(COD)]BF_4, **10^{maj}**, in acetone-d_6 as determined by 2DCPA. The absolute configuration of **10^{maj}** is shown, along with labels for all carbon atoms. Selected H's are also labeled, particularly those involved in the NOE interactions which allowed for the structure determination.

The assignment of the ^{1}H NMR was aided by our elucidation of the ^{13}C NMR of **10^{maj}**. The ^{13}C NMR was quite well dispersed, and only the region from 34.3 to 34.7 ppm contained significant overlap. Correlation of the ^{1}H and ^{13}C resonances was achieved with a ^{1}H−^{13}C HMQC (heteronuclear correlation through multiple quantum coherence) experiment. The ^{13}C assignments are given in Table 5. Overlap in the ^{13}C dimension did not allow for the assignment of all individual CH_2 carbons in the phospholane rings and CH carbons in the phenyl ring. Assigning the structure of **10^{min}** has been complicated by overlap of its methylene and methyl regions with the major species **10^{maj}**.

Solution Structure Determination of 10^{maj} by Conformer Population Analysis. The solution structure of the major diastereomer **10^{maj}** was determined by analyzing the time course of the quantitative ^{1}H 2D NOESY data with the multiconformational analysis technique, two-dimensional conformation population analysis (2DCPA).[21,29−31] This method requires the quantitation of NOESY time courses. Initial experiments in CD_2Cl_2 at −80 °C were not useable, because both positive and negative NOE enhancements were observed, indicating that the isotropic rotational correlation times corresponded to the null region of NOE enhancement. The NOESY data collected in acetone-d_6 at −90 °C (mixing times of 70, 100, 130, 160, and 200 ms) resulted in enhanced, negative NOEs.

(29) Landis, C.; Allured, V. S. *J. Am. Chem. Soc.* **1991**, *113*, 9493−9499.
(30) Landis, C. R.; Luck, L. L.; Wright, J. M. *J. Magn. Reson. Ser. B* **1995**, *109*, 44−59.
(31) Casey, C. P.; Hallenbeck, S. L.; Wright, J. M.; Landis, C. R. *J. Am. Chem. Soc.* **1997**, *119*, 9680.

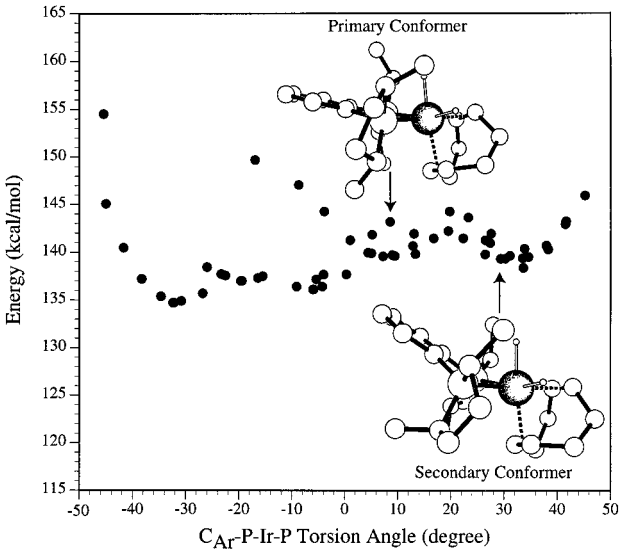

Figure 6. Molecular mechanics energies of all conformers used in the 2DCPA analysis. The two conformers obtained by quantitative analysis of the NOE data are illustrated.

The 2DCPA analysis correlates the observed NOESY intensities or the experimental cross-relaxation rates at each mixing time to the calculated NOE data from a set of energetically reasonable trial models created by molecular mechanics.[21,29−31] Unlike the single, average solution approach, the best representation of 2DCPA solution structures is given by the smallest combination of statistically significant conformers and their populations. The goal of this 2DCPA analysis is to investigate the detailed structure in space of the major diastereomer of the dihydride complexes **10^{maj}**. Our analysis involved three steps: (1) collection of NOESY time courses, (2) creation of an ensemble of trial solution structures using molecular mechanics, and (3) conformer population analysis of the observed NOESY time courses to find the smallest combination of the trial structures and their populations. The details of this analysis are provided in the Experimental Section.

Quantitative analysis of the NOE data confirms the assignment of absolute stereochemistry of **10^{maj}** in solution. The structure of **10^{maj}** is highly constrained by the multiple ring elements. The primary conformational degree of freedom corresponds to the orientation of the bridging phenylene ring with respect to the hydride ligand which is cis to both phosphorus atoms, which we will call the axial hydride. Our analysis of the NOE time courses finds that the most likely conformation has the plane of the phenylene ring essentially coplanar with the plane defined by the two P and the Ir atoms. This structure is shown in Figures 5 and 6. Statistically, the data are fit significantly better when two conformations are used; the secondary conformer is shown in Figure 6. The secondary conformer has the phenylene ring rotated toward the axial hydride. According to molecular mechanics computations, both conformers have energies within 9 kcal/mol of the lowest energy conformation (see Figure 6).

Kinetic Studies of Isotope Exchange and Diastereomer Interconversion of [IrH$_2$(COD)(Me-DuPHOS)]BF$_4$. The dynamics of dihydride diastereomer interconversion are potentially important in determining the selectivities of catalytic asymmetric hydrogenation reactions. Several possible mechanisms for dihydride diastereomer interconversion are shown in Figure 7. In the [IrH$_2$(COD)(Me-DuPHOS)]BF$_4$ system, the diastereomer interconversion is an approach to equilibrium. To simplify, we will refer to this approach to equilibrium as "diastereomer exchange".

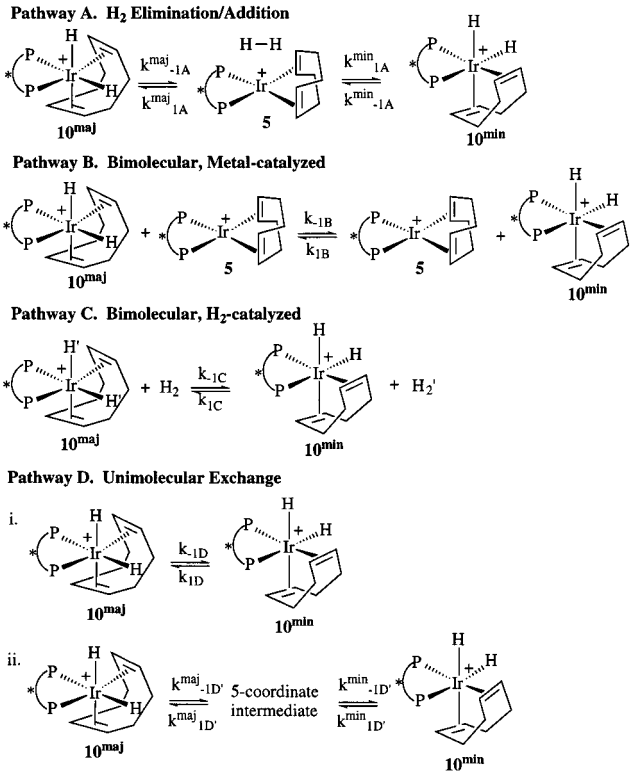

Figure 7. Pathways for the mechanism of diastereomer interconversion for [IrH$_2$(Me-DuPHOS)(COD)]BF$_4$.

For pathway A, the rate of diastereomer interconversion should be first order in $[Ir]_{tot}$ and independent of the H_2 concentration. Pathway B is kinetically distinguishable from all other pathways because it leads to a rate of diastereomer interconversion that is second order in $[Ir]_{tot}$. Based on the high thermodynamic stability of the dihydride complexes, **10^{maj}** and **10^{min}**, pathway B should exhibit an inverse dependence on the $[H_2]$ because the concentration of the four-coordinate catalyst concentration decreases with increasing $[H_2]$. Pathway C requires a first-order dependence of the diastereomer interconversion on $[H_2]$. Kinetically, pathway D is indistinguishable from pathway A. However, isotopic scrambling results discriminate between pathways A and D (vide infra).

The diastereomer exchange of [IrH$_2$(Me-DuPHOS)(COD)]BF$_4$ at −45 °C was monitored by ^{1}H NMR or ^{31}P NMR as a function of $[Ir]_{tot}$ and P_{H_2} (Table 6). Within the precision of the data, the rate is invariant of the $[Ir]_{tot}$ and P_{H_2}. Thus, pathways B and C are inconsistent with the observed kinetics.

Isotope exchange experiments (Figure 8) of H_2 with d_2-**10^{maj}** and d_2-**10^{min}** permit discrimination between pathways A and D. *If pathway A is operative, the exchange of H_2 with d_2-**10^{maj}** must occur more rapidly than the equilibration of **10^{maj}** with **10^{min}***. Each time D_2 is eliminated from d_2-**10^{maj}** under an atmosphere of H_2, isotope exchange will occur by the subsequent addition of H_2. The reaction of H_2 with [Ir(COD)(Me-DuPHOS)]$^+$ at −45 °C is kinetically biased to produce **10^{maj}** at least 10 times faster than **10^{min}**. Therefore, for 10 occurrences of D_2 elimination from d_2-**10^{maj}**, at most only one will lead to diastereomer interconversion (i.e., produce d_2-**10^{min}**), but all 10 will lead to H_2 incorporation. The observation of near equivalent rates for diastereomer interconversion and incorporation of H_2 into a solution initially consisting of >97% d_2-**10^{maj}** (Table 6) precludes significant flux along pathway A.

Table 6. Kinetic Studies of Diastereomer Interconversion and Isotope Exchange for [IrH_2(Me-DuPHOS)(COD)]BF_4 (**10**)

experiment	solvent	observed nucleus	[Ir] (mM)	P_{H_2} (atm)	T (°C)	$t_{1/2}$ (min)
10^{maj} ⇌ **10^{min}**	CD_2Cl_2	^{1}H	27	0	−45	47 ± 10
10^{maj} ⇌ **10^{min}**	CD_2Cl_2	^{1}H	55	0	−45	47 ± 10
10^{maj} ⇌ **10^{min}**	CD_2Cl_2	^{31}P	55	1	−45	43 ± 10
10^{maj} ⇌ **10^{min}**	CD_2Cl_2	^{31}P	27	0.083	−45	62 ± 12
10^{maj} ⇌ **10^{min}**	acetone-d_6	^{1}H	35	0	−45	64 ± 12
d_2-**10^{maj}** + H_2	CD_2Cl_2	^{1}H	55	1	−45	47 ± 10
d_2-**10^{maj}** + H_2	CD_2Cl_2	^{1}H	27	0.083	−45	51 ± 10
d_2-**10^{maj}** (H incorporation into M−D)	CD_2Cl_2	^{1}H	27	0	−45	52 ± 10
d_2-**10^{maj}** (H incorporation into M−D)	acetone-d_6	^{1}H	35	0	−45	55 ± 12
d_2-**10^{maj}** (D incorporation into H1 and H25A)	CD_2Cl_2	^{2}H	52	0	−45	56 ± 12

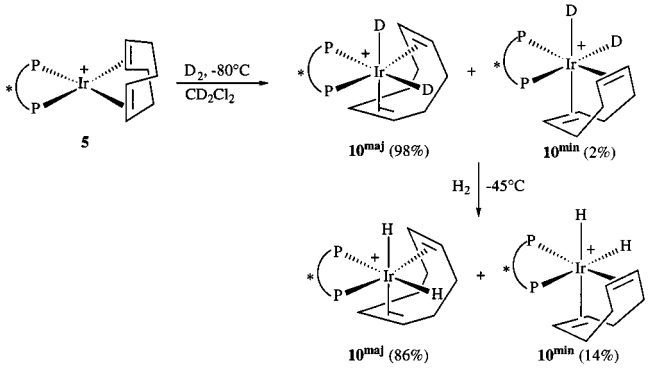

Figure 8. Isotope exchange experiment for [IrD_2(Me-DuPHOS)(COD)]-BF_4 (**10**).

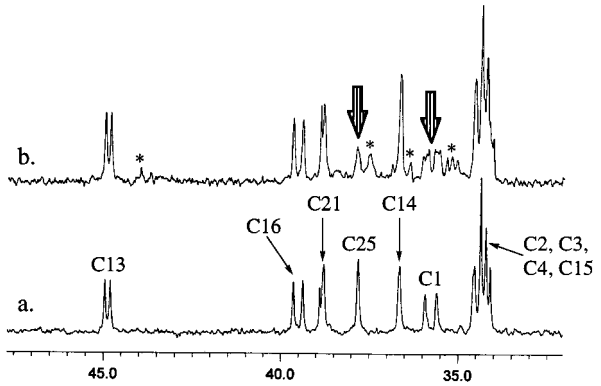

Figure 9. The 126-MHz ^{13}C NMR spectra of [IrD_2(Me-DuPHOS)-(COD)]BF_4 at −80 °C (a) right after formation of the dihydride at −80 °C and (b) after deuterium incorporation into sites on C25 and C1 after equilibration at −45 °C. Deuterium incorporation sites are indicated with large arrows, and asterisks indicate peaks which are due to **10^{min}**.

By elimination, only pathway D of the four pathways illustrated in Figure 7 is consistent with the observed data (we note that other, more complicated pathways are possible). These results contrast Deutsch and Eisenberg's identification of diastereomer exchange pathways similar to A and B for Ir(diphosphine)(CO)X (X = halide) complexes.[20]

A surprising result of our investigations was the observed growth of M−H resonances from solutions of d_2-**10^{maj}** and d_2-**10^{min}**, even in the absence of added H_2. Because there was no net decomposition of the dihydride complexes and the solvent was perdeuterated, this result suggests that H and D are exchanged among M−H and ligand C−H sites. Confirmation of such exchange is provided by ^{2}H NMR and ^{13}C NMR experiments. A solution of d_2-**10^{maj}** at −45 °C under N_2 yields growth of two broad resonances at δ 2.5 and 2.8 ppm in the ^{2}H NMR spectrum and decay of the M−D resonances at δ −9.8 to −15.7 ppm. After approximately 4 h, the resonance intensities cease to change, indicating that equilibrium has been reached. At equilibrium, the ratio of D resonance intensities for total M−D versus total C−D is 1.3 ± 0.4. Apparently, there is no substantial isotope effect. The half-life for this approach to equilibrium is similar to those for isotope label exchange under an H_2 atmosphere and for diastereomer interconversion. There is no apparent difference in the rates of deuterium label scrambling for the two diastereomers, as determined from comparison of diastereomer ratios measured by ^{31}P NMR with the ratio of hydride resonances (major:minor) determined by ^{1}H NMR.

Due to the broadness of the ^{2}H NMR resonances, ^{13}C NMR was employed to determine which ligand sites were exchange active. The decrease in intensity and broadening of peaks at δ 35.76 (d, J_{P-H} = 41 Hz) and 37.89 (s) ppm in the ^{13}C NMR (Figure 9) demonstrates exclusive (within sensitivity limits) incorporation of deuterium into the COD methylene (C25) and the Me-DuPHOS methine (C1) positions. These changes are consistent with approximately 50% exchange of D with H25A and H1. Therefore, exchange of M−D with ligand C−H bonds is exquisitely selective.

Given the constraints of the rate data for diastereomer and isotope exchange, it is difficult to construct a simple mechanism. The primary issues are (1) why are the isotope exchange rates and diastereomer exchange rates equal (within experimental resolution), and (2) why does isotope exchange proceed exclusively into two ligand C−H bonds? We favor variant ii of pathway D, in which the primary kinetic event corresponds to formation of a five-coordinate intermediate. Three reasonable five-coordinate intermediates are (1) a formally Ir(I) molecular hydrogen complex, (2) a formally Ir(III) complex with a dangling diphosphine ligand, and (3) a formally Ir(III) complex with a dangling COD ligand. The latter two are coordinatively unsaturated, 16-electron complexes which might be expected to activate ligand C−H bonds to isotope exchange via oxidative addition, yielding 18-electron Ir(V) complexes. One possible scheme is detailed in Figure 10 below.

For simplicity of discussion, it is easiest to focus on the formation of **10^{maj}** and **10^{min}** from essentially pure d_2-**10^{maj}** under a H_2 atmosphere. Conversion of **10^{maj}** to **17^{maj}** via decoordination of the C═C bond located cis to the Ir−D bond is slow. From coordinatively unsaturated **17^{maj}**, oxidative addition of the allylic C−H bond yields an η^3-allyl trihydride (**18^{maj}**). Subsequent elimination of HD forms the η^3-allyl monohydride (**19**) and provides an entry for scrambling with external H_2 or D_2. Conversion to the minor diastereomer may occur in two ways: by rotation about the Ir−allyl centroid of **10^{maj}** to generate **10^{min}** followed by insertion of the allyl into Ir−D bond to yield **17^{min}**, or by readdition of HD to **19** (after rotation about the Ir−allyl centroid). A similar mechanism (not shown) scrambles Ir−D with the methine C−H of the diphosphine ligand. From the coordinatively unsaturated **17^{maj}**, oxidative addition of the methine C−H bond to form an

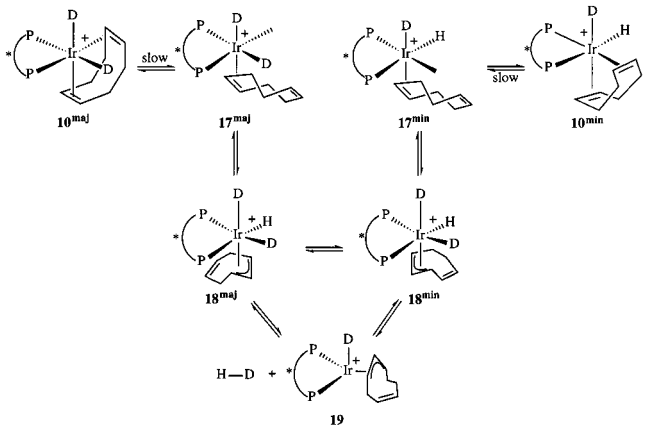

Figure 10. Proposed mechanism of diastereomer interconversion and isotopomer exchange for $[IrD_2(Me\text{-}DuPHOS)(COD)]BF_4$ (**10**).

iridaphosphacyclopropane trihydride (**20**) permits the requisite D-scrambling and diastereomer interconversion processes.

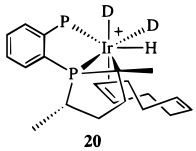

The virtues of this mechanistic proposal are that it (1) yields similar rates for approach to equilibrium of both diastereomer interconversion and isotope exchange, (2) accounts for independence of these rates on H_2 pressure and $[Ir]_{tot}$, (3) yields similar H−D isotope ratios for both the major and minor diastereomers throughout the diastereomer interconversion process, and (4) accounts for highly selective incorporation of D into just two ligand sites. Evidence for this type of a mechanism could be found by trapping the intermediate **17** with a ligand such as $P(OMe)_3$. Unfortunately, the phosphite was not a good trap for this reaction and gave rise to complexes which contained neither hydrides nor cyclooctadiene.

Conclusion

The examination of the formation and dynamics of iridium dihydrides provides useful insights into the selectivity of authentic H_2 oxidative addition reactions. Our studies conclusively demonstrate that the kinetic and thermodynamic selectivities of oxidative addition are not the same. Indeed, for at least one complex, $[Ir(CHIRAPHOS)(COD)]^+$, the thermodynamic and kinetic selectivities of dihydrogen oxidative addition have the opposite sense. As a result, one cannot expect models of dihydride stabilities derived from, for example, molecular mechanics, to necessarily mirror the diastereoselectivity of the oxidative addition transition states. Thus, it is not surprising that previous molecular modeling studies of putative dihydride intermediates in catalytic asymmetric hydrogenation of enamides failed to find significant differences in stabilities between the diastereomeric dihydrides.[21] For the $[IrH_2(Me\text{-}DuPHOS)(COD)]^+$ complexes studied here, we have been able to establish the solution structures, including the absolute configuration, using NOESY methods and the 2DCPA program. The kinetically preferred dihydride diastereomer is that in which the COD ligand is twisted in the same direction as is seen in the distorted square planar geometry of the reactant $[Ir(Me\text{-}DuPHOS)(COD)]^+$. However, one must be cautious in extending this explanation to control of the enantioselectivity of enamide hydrogenation: the extent of diastereoselectivity observed for addition of H_2 to $[Ir(chiral\ diphosphine)(COD)]^+$ complexes does not correlate well with enamide enantioselectivities.

The diastereomeric dihydrides exhibit surprisingly facile interconversion and deuterium scrambling pathways. These pathways do not involve reductive elimination of dihydrogen to regenerate the square planar, four-coordinate starting complex. The significance of these mechanistic results is that they demonstrate the potential complexity of the dynamics of dihydride intermediates.

Experimental Section

General Procedures. All procedures were carried out under a dry atmosphere of nitrogen by using standard Schlenk techniques and an inert atmosphere glovebox. Glassware was oven-dried before use. Nitrogen (Liquid Carbonic), hydrogen (Liquid Carbonic), 8.3% hydrogen (balance N_2, Liquid Carbonic), and deuterium (Cambridge Isotope) were used without further purification. NMR solvents, CD_2Cl_2 and acetone-d_6, were used as obtained from Cambridge Isotope and Isotech Inc., respectively. Methylene chloride was distilled from P_2O_5, and acetone was dried over molecular sieves and distilled. Diethyl ether was freshly distilled from sodium/benzophenone ketyl.

$IrCl_3$ was obtained from Johnson-Mathey. $[Ir(COD)Cl]_2$[32] and $Ir(COD)_2]BF_4$[33] were prepared according to literature procedures. (*R*)-BINAP, (*R*,*R*)-NORPHOS, (*R*)-Tol-BINAP, (*S*,*S*)-CHIRAPHOS, and (*R*,*R*)-Me-DuPHOS were used as received from Strem Chemicals. (*S*,*R*)-BPPFAc and (*S*,*R*)-BPPFA were prepared according to literature procedures.[34]

Low-temperature ^1H NMR (500 MHz), $^2H\{^1H\}$ NMR (76 MHz), $^{31}P\{^1H\}$ NMR (202 MHz), and $^{13}C\{^1H\}$ NMR (126 MHz) were performed on a Bruker AM-500 spectrometer. Room-temperature ^1H NMR (300 MHz) and $^{31}P\{^1H\}$ NMR (121 MHz) were taken on a Bruker AC-300 spectrometer. ^1H DQF COSY and NOESY NMR were performed on a Varian Unity-500 spectrometer with a 5-mm $^1H/^{19}F$ probe. $^1H/^{13}C$ HMQC NMR was performed on a Varian Unity-500 spectrometer with a 5-mm inverse broadband probe. Probe temperatures were calibrated using a methanol standard.

[Ir(P−P)(COD)]BF_4 Preparation. $[Ir(P-P)(COD)]BF_4$ complexes were prepared in situ from $[Ir(COD)_2]BF_4$, a deep purple solid, and the corresponding bisphosphine. $[Ir(COD)_2]BF_4$ was found to decompose as a solid, even when stored at 0 °C in the absence of light, and should be used soon after preparation.

[Ir(COD)((*S*,*S*)-DIOP)]BF_4 (1). A solution of (*S*,*S*)-DIOP (10.0 mg, 2.0×10^{-5} mol, 1 equiv in 0.5 g of CD_2Cl_2) was added dropwise to a solution of $[Ir(COD)_2]BF_4$ (9.9 mg, 2.0×10^{-5} mol, 1 equiv in 0.5 g of CD_2Cl_2), yielding a bright red solution. Data for $[Ir((S,S)\text{-}DIOP)(COD)]BF_4$ (**1**) at room temperature: ^1H NMR (CD_2Cl_2, 300 MHz) δ 1.09 (m, 6H, CH_3), 1.87−2.35 (m, 17H, free and bound COD CH_2's), 2.70 (m, DIOP CH_2's), 3.13 (m, DIOP CH_2's), 3.80 (m, 2H, DIOP CH's), 4.00 (m, 2H, bound COD vinyl), 4.23 (m, 2H, bound vinyl), 5.55 (m, 4H, free COD vinyls), 7.27−7.67 (m, 20H, phenyls) ppm; ^{31}P NMR (CD_2Cl_2, 121 MHz) δ 4.8 (s) ppm.

[Ir((*S*,*S*)-CHIRAPHOS)(COD)]BF_4 (2). A solution of (*S*,*S*)-CHIRAPHOS (9.6 mg, 2.3×10^{-5} mol, 1 equiv in 0.5 g of CD_2Cl_2) was added dropwise to a solution of $[Ir(COD)_2]BF_4$ (11.2 mg, 2.3×10^{-5} mol, 1 equiv in 0.5 g of CD_2Cl_2), yielding a deep green solution. ^1H and $^{31}P\{^1H\}$ NMR for $[Ir((S,S)\text{-}CHIRAPHOS)(COD)]BF_4$ (**2**) at room temperature were consistent with previously published results:[15] ^1H NMR (CD_2Cl_2) δ 1.06 (m, 6H, CH_3), 1.75−1.98 (m, 4H, COD CH_2), 2.15−2.55 (m, 14H, 2 CH's and free and bound COD CH_2), 4.02 (m, 2H, bound COD vinyls), 4.82 (m, 2H, bound COD vinyl), 5.55 (m, 4H, free COD), 7.38−7.86 (m, 20H, phenyl) ppm; $^{31}P\{^1H\}$ NMR δ 46.4 ppm.

(32) Crabtree, R. H.; Quirk, J. M.; Felkin, H.; Fillebeen-Khan, T. *Synth. React. Inorg. Met.-Org. Chem.* **1982**, *12*, 407.

(33) Schenck, T. G.; Downes, J. M.; Milne, C. R. C.; MacKenzie, P. B.; Boucher, H.; Whelan, J.; Bosnich, B. *Inorg. Chem.* **1985**, *24*, 2334.

(34) Hayashi, T.; Mise, T.; Fukushima, M.; Kagotani, M.; Nagashima, N.; Hamada, Y.; Matsumoto, A.; Kawakami, S.; Konishi, M.; Yamamoto, K.; Kumada, M. *Bull. Chem. Soc. Jpn.* **1980**, *53*, 1138.

Table 7. Crystallographic Data for [Ir((*R*,*R*)-Me-DuPHOS)(COD)]BF_4 (**5**)

formula	$[C_{26}H_{40}IrP_2]^+[BF_4]^-$	ρ_{calc}, g cm^{-3}	1.709
fw	693.53	*T*, K	133(2)
cryst color, habit	brown opaque needle	*F*(000)	1376
cryst size, mm	0.50 × 0.10 × 0.10	radiation; λ, Å	Mo Kα; 0.710 73
cryst syst	orthorhombic	diffractometer	Siemens P4/CCD
space group	$P2_12_12_1$	2θ(max), deg	58.4
a, Å	9.1569(2)	no. reflctns collected	12 902
b, Å	16.0222(2)	no. reflctns used	6419
c, Å	18.3723(3)	no. params refined	307
$\alpha = \beta = \gamma$	90°	*R*(*F*), observed data	0.018
V, Å^3	2695.47(8)	w*R*(F^2), all data	0.045
Z	4	goodness of fit on F^2	1.038

[Ir((*R*)-BINAP)(COD)]BF_4 (3). A solution of (*R*)-BINAP (12.6 mg, 2.0 × 10^{-5} mol, 1 equiv in 0.5 g of CD_2Cl_2) was added dropwise to a solution of [Ir(COD)$_2$]BF_4 (10.0 mg, 2.0 × 10^{-5} mol, 1 equiv in 0.5 g of CD_2Cl_2), yielding a very dark red solution. Data for [Ir((*R*)-BINAP)(COD)]BF_4 (**3**) at room temperature: ^{1}H NMR (300 MHz, CD_2Cl_2) δ 1.80−1.96 (m, 3H, bound COD CH_2's), 2.07−2.41 (m, 13H free COD and bound CH_2's), 4.24 (m, 2H, bound vinyl), 4.47 (m, 2H, bound vinyl), 5.55 (m, 4H free COD vinyl), 6.46−7.90 (m, 32H, phenyls) ppm; ^{31}P NMR (CD_2Cl_2) δ 17.8 (s) ppm.

[Ir(COD)((*R*)-Tol-BINAP)]BF_4 (4). A solution of (*R*)-Tol-BINAP (10.9 mg, 1.6 × 10^{-5} mol, 1 equiv in 0.5 g of CD_2Cl_2) was added dropwise to a solution of [Ir(COD)$_2$]BF_4 (8.0 mg, 1.6 × 10^{-5} mol, 1 equiv in 0.5 g of CD_2Cl_2), yielding a brown-green solution. Data for [Ir((*R*)-Tol-BINAP)(COD)]BF_4 (**4**) at room temperature: ^{1}H NMR (300 MHz, CD_2Cl_2) δ 1.76 (br s, 2H, bound COD CH_2's), 1.90 (s, 6H, 2 CH_3's), 2.28 (br s, 2H, bound COD CH_2's), 2.16−2.42 (m, 20H, free and bound COD CH_2's, 2 CH_3's), 4.16 (br s, 4H, bound COD vinyls), 5.49 (br s, 4H, free COD vinyl), 6.06−7.83 (m, 28H, phenyls) ppm; ^{31}P NMR (CD_2Cl_2) δ 16.5 (s) ppm.

[Ir((*R*,*R*)-Me-DuPHOS)(COD)]BF_4 (5). A solution of (*R*,*R*)-Me-DuPHOS (6.2 mg, 2.0 × 10^{-5} mol, 1 equiv in 0.5 g of CD_2Cl_2) was added dropwise to a solution of [Ir(COD)$_2$]BF_4 (10.0 mg, 2.0 × 10^{-5} mol, 1 equiv in 0.5 g of CD_2Cl_2), yielding a deep brown solution. Assignments for [Ir((*R*,*R*)-Me-DuPHOS)(COD)]BF_4 (**5**) are listed below for the isolated complex. Procedures for the isolation of [Ir((*R*,*R*)-Me-DuPHOS)(COD)]BF_4 are also given below.

[Ir((*R*,*R*)-NORPHOS)(COD)]BF_4 (11). A solution of (*R*,*R*)-NORPHOS (15.0 mg, 3.2 × 10^{-5} mol, 1 equiv in 0.5 g of CD_2Cl_2) was added dropwise to a solution of [Ir(COD)$_2$]BF_4 (16.0 mg, 3.2 × 10^{-5} mol, 1 equiv in 0.5 g of CD_2Cl_2), yielding a deep brown-green solution (**11**). ^{1}H and ^{31}P{^{1}H} NMR were consistent with previously published results:[15] ^{1}H NMR (500 MHz, CD_2Cl_2, −80 °C) δ 0.78 (d, 1H, *J* = 8 Hz, NORPHOS bridging CH_2), 1.53 (m, 2H, bound CH_2 COD), 1.78 (m, 3H, bound CH_2 COD and NORPHOS bridging CH_2), 2.30−2.60 (m, 13H, free COD, 4 bound COD CH_2, and 1 C*H*PPh_3), 2.69 (m, 1H, NORPHOS bridgehead), 3.00 (m, 1H, NORPHOS bridgehead), 3.06 (m, 1H, C*H*PPh_3), 3.76 (m, 2H, bound COD vinyl), 4.85 (m, 2H, bound COD vinyl), 5.35 (m, 1H, NORPHOS vinyl), 5.53 (m, 4H, free COD vinyl), 6.10 (m, 1H, NORPHOS vinyl), 7.32−7.75 (m, 20H, phenyl) ppm; ^{31}P NMR (CD_2Cl_2, 202 MHz, −80 °C) δ 11.1 (d, *J* = 15 Hz), 12.2 (d, *J* = 15 Hz) ppm.

[Ir((*S*,*R*)-BPPFA)(COD)]BF_4 (12). A solution of (*R*,*R*)-BPPFA (12.9 mg, 2.1 × 10^{-5} mol, 1 equiv in 0.5 g of CD_2Cl_2) was added dropwise to a solution of [Ir(COD)$_2$]BF_4 (10.2 mg, 2.1 × 10^{-5} mol, 1 equiv in 0.5 g of CD_2Cl_2), yielding a bright red solution. Data for [Ir((*S*,*R*)-BPPFA)(COD)]BF_4 (**12**) at room temperature: ^{1}H NMR (300 MHz, CD_2Cl_2) δ 1.22 (d, 3H, *J* = 6.3 Hz, CHC*H*$_3$), 1.76−1.95 (m, 4H, bound COD CH_2's), 2.13−2.43 (m, 18H, free and bound COD CH_2's and N(CH_3)$_2$), 3.79 (br s, 1H, 1 Cp), 4.04−4.59 (m, 12H, bound COD vinyls, Cp's and C*H*CH_3), 5.55 (br s, 4H, free COD vinyl), 7.31−7.99 (m, 20H, phenyls) ppm; ^{31}P NMR (CD_2Cl_2) δ 15.7 (d, J_{P-H} = 16 Hz), 21.3 (br s) ppm.

[Ir(COD)((*S*,*R*)-BPPFAc)]BF_4 (13). A solution of (*R*,*R*)-BPPFAc (13.1 mg, 2.1 × 10^{-5} mol, 1 equiv in 0.5 g of CD_2Cl_2) was added dropwise to a solution of [Ir(COD)$_2$]BF_4 (10.2 mg, 2.1 × 10^{-5} mol, 1 equiv in 0.5 g of CD_2Cl_2), yielding a bright red solution. Data for [Ir(COD)((*S*,*R*)-BPPFAc)]BF_4 (**13**) at room temperature: ^{1}H NMR (300 MHz, CD_2Cl_2) δ 1.50 (d, 3H, *J* = 6.0 Hz, CHC*H*$_3$), 1.75−1.94 (m, 4H, bound COD CH_2's), 2.00 (s, 3H, OAc), 2.11−2.55 (m, 12H, free and bound COD), 3.98−4.51 (m, 10H, Cp's and bound COD vinyls), 4.82 (m, 1H, 1 Cp), 5.55 (br s, 4H, free COD vinyl), 6.45 (q, *J* = 6.0 Hz, C*H*CH$_3$), 7.32−8.11 (m, 20H, phenyls); ^{31}P NMR (CD_2Cl_2) δ 14.5 (d, J_{P-H} = 16 Hz), 17.7 (d, J_{P-H} = 16 Hz) ppm.

[Ir(COD)((*R*,*R*)-Me-DuPHOS)]BF_4 (5) Isolation. [Ir(COD)$_2$]BF_4 (300.0 mg, 0.605 mmol) was placed into a Schlenk flask and dissolved in 30 mL of freshly distilled CH_2Cl_2. A solution of (*R*,*R*)-Me-DuPHOS (185.5 mg, 0.605 mmol, 1 equiv) in CH_2Cl_2 (30 mL) was added dropwise over 15 min. The solution volume was reduced to approximately 5 mL, and the solution was layered with 10 mL of freshly distilled diethyl ether. Brown needles formed overnight in the absence of light (254 mg, 0.366 mmol, 61% yield): ^{1}H NMR (300 MHz, CD_2Cl_2) δ 1.01 (dd, 6H, *J* = 15.0, 6.9 Hz, CH_3), 1.36 (dd, 6H, *J* = 18.0, 7.0 Hz, CH_3), 1.64 (m, 2H, *J* ≈ 13.2, 4.8, 2.4 Hz, CH_2), 1.93 (m, 2H, *J* ≈ 12.9, 4.8 Hz, CH_2), 1.75−2.53 (m, 14H, COD CH_2's), 2.92 (m, 2H, *J* ≈ 6.8 Hz, CH), 4.60 (m, 2H, COD vinyl), 5.29 (m, 2H, vinyl), 7.67−7.78 (m, 4H, phenyl) ppm; ^{31}P NMR (121 MHz, CD_2Cl_2) δ 68.6 ppm. Assignments were made using a COSY-45, which was collected using standard pulse sequences.[35,36]

Crytallographic Structure Determination of [Ir(COD)((*R*,*R*)-Me-DuPHOS)]BF_4 (5). A single crystal was grown from CH_2Cl_2/diethyl ether. Crystal data are summarized in Table 7. A total of 12 902 reflections with 2θ < 58.4° were collected on a Siemens P4/CCD diffractometer using graphite-monochromated Mo Kα radiation. The structure was solved by direct methods and was refined by full-matrix least squares on F^2 values with hydrogens riding.[37,38] Non-hydrogen atoms were refined with anisotropic thermal parameters. The final *R*(*F*) and w*R*(F^2) factors were 0.018 and 0.045, respectively. The crystal structure is shown in Figure 4, along with a partial numbering scheme. Selected bond lengths and bond angles are given in Table 7. Fractional coordinates and additional crystallographic data can be found in the Supporting Information.

In Situ Generation of [IrH_2(P−P)(COD)]BF_4. [IrH_2(P−P)(COD)]BF_4 complexes were formed by bubbling cold dihydrogen (−80 °C) through a solution of [Ir(P−P)(COD)]BF_4 at −80 °C. This reaction was almost immediate and was accompanied by a color change. The reactions were followed by ^{31}P NMR and the hydride region of the ^{1}H NMR (Tables 1 and 5). Product ratios were determined by ^{31}P and ^{1}H NMR (see Table 2). The full NMR spectra are available in the Supporting Information.

[IrH_2(P−P)(COD)]BF_4 Warming Experiments. Solutions of [IrH_2(P−P)(COD)]BF_4 at −80 °C were warmed to −45 °C (acetonitrile/N_2 bath) for periods of 2−5 h. These solutions were cooled to −80 °C, and their ^{31}P and ^{1}H NMR were recorded. Results are given in Table 2. Further experimental details have been published in the thesis of B. F. M. Kimmich.[39]

(35) Freeman, R.; Morris, G. A. *Bull. Magn. Reson.* **1979**, *1*, 1.
(36) Bax, A.; Freeman, R. *J. Magn. Reson.* **1981**, *44*, 542.
(37) *SAINT Version 4 Software Reference Manual*; Siemens Analytical X-ray Instruments: 6300 Enterprise Dr., Madison, WI 53719-1173; 1995.
(38) Sheldrick, G. M. *SHELXTL VERSION 5 Software Manual*; Siemens Analytical X-ray Instruments: 6300 Enterprise Dr., Madison, WI 53719-1173; 1995.
(39) Kimmich, B. F. M. Ph.D. Dissertation, University of Wisconsin−Madison, 1998.

NMR Characterization of [IrH_2((*R,R*)-Me-DuPHOS)(COD)]BF_4 (10^{maj}). A 50 mM solution of [Ir((*R,R*)-Me-DuPHOS)(COD)]BF_4 (**5**) in CD_2Cl_2 was cooled to −80 °C (dry ice/acetone). A steady stream of cold (−80 °C) H_2 was bubbled through the deep brown solution for about 5 min. A pale yellow solution was formed, >98% by NMR as above. ^{1}H, ^{13}C, and ^{31}P NMR data for [IrH_2(COD)((*R,R*)-Me-DuPHOS)]BF_4 are given in Tables 1 (^{31}P NMR) and 5 (^{1}H and ^{13}C NMR). All data were acquired at −80 °C. A combination of DQF COSY and NOESY spectra was used to assign the ^{1}H NMR. The DQF COSY and NOESY spectra are provided in the Supporting Information. The ^{13}C NMR, DEPT 135, and HMQC NMRs were used to assign the carbon atoms for $\mathbf{10^{maj}}$. Due to overlap in the ^{13}C dimension of the HMQC, two sets of carbon peaks could not be completely assigned. Four carbons are overlapped at 34.3 ppm, corresponding to three CH_2 and one CH carbons on the phospholane rings. Two phenyl carbons at 130.4 ppm also could not be differentiated.

A 500-MHz ^{1}H−^{1}H DQF COSY was obtained at −80 °C in CD_2Cl_2. The spectrum was gathered using a phase-sensitive DQF COSY pulse sequence[40,41] with an initial homospoil pulse and States−Haberkorn−Ruben phase cycling.[42] A data set with t_1 and t_2 dimensions of 512 and 2048 real points, respectively, was collected using relaxation delays of 3.5 s for eight scans of each FID. The Felix NMR software package from Molecular Simulations, Inc. was used to transform and process the data. t_1 was zero-filled to 1024 points, and t_2 was zero-filled to 4096 points. The complete ^{1}H−^{1}H DQF COSY spectrum is available in the Supporting Information.

A 500-MHz ^{1}H NOESY was obtained at −80 °C in CD_2Cl_2 with a mixing time of 300 ms. The spectrum was gathered using a phase-sensitive 2D-NOESY pulse sequence[43] with an initial homospoil pulse and States−Haberkorn−Ruben phase cycling.[42] A data set with t_1 and t_2 dimensions of 512 and 2048 real points, respectively, was collected using relaxation delays of 3.5 s for eight scans of each FID. The Felix NMR software package from Molecular Simulations, Inc. was used to transform and process the data. t_1 was zero-filled to 1024 points, and t_2 was zero-filled to 4096 points. The complete ^{1}H−^{1}H NOESY spectrum is available in the Supporting Information.

A 500-MHz ^{1}H−^{13}C HMQC was obtained at −80 °C in CD_2Cl_2. The spectrum was gathered using a HMQC pulse sequence.[44,45] A data set with t_1 and t_2 dimensions of 512 and 2048 real points, respectively, was collected using relaxation delays of 1.5 s for 24 scans of each FID. The VNMR software package from Varian Nuclear Magnetic Resonance Instruments was used to transform and process the data. t_1 was zero-filled to 1024 points, and t_2 was zero-filled to 4096 points. The complete ^{1}H−^{13}C HMQC spectrum is available in the Supporting Information.

Determination of the Solution Structure of 10^{maj}. A 36 mM solution of [Ir((*R,R*)-Me-DuPHOS)(COD)]BF_4 was prepared in acetone-d_6. The solution was reacted with H_2 at −80 °C and warmed to −45 °C, yielding a 5.8:1.0 mixture of dihydrides $\mathbf{10^{maj}}$ and $\mathbf{10^{min}}$. All 2D experiments were acquired at −90 °C.

^{1}H DQF COSY NMR Experiments. The spectrum was measured using a phase-sensitive DQF COSY pulse sequence[40,41] with an initial homospoil pulse and States−Haberkorn−Ruben phase cycling at −90 °C in acetone-d_6.[42] A total of 1024 increments of eight scans was collected with 2048 real points in t_2. The relaxation delay was set to 1.5 s. The Felix NMR software package was used to transform and process data. t_1 was zero-filled to 2048 points, and t_2 was zero-filled to 4096 points. A linear prediction scheme was used to correct the first point and generate points at the tails of the FID, extending data by one-third. Gaussian linebroadening and a screwed sine-squared bell were applied to the FID.

^{1}H NOESY NMR Experiments. Spectra were obtained at −90 °C in acetone-d_6. Spectra were collected at 70, 100, 130, 160, and 200 ms mixing times using a phase-sensitive NOESY pulse sequence[43] with an initial homospoil pulse and States−Haberkorn−Ruben phase cycling.[42] A total of 1024 increments of eight scans was collected with 2048 real points in t_2. The relaxation delay was set to 1.5 s. The Felix NMR software package was used to transform and process data. t_1 was zero-filled to 2048 points, and t_2 was zero-filled to 4096 points. A linear prediction scheme was used to correct the first point and generate points at the tails of the FID, extending data by one-third. A Kaiser window function and exponential linebroadening were applied to the FID to reduce apodization artifacts. Low-order polynomial baseline corrections were applied to each dimension. The baselines were corrected again using FACELIFT from the National Magnetic Resonance Facility at Madison and deconvolution facility in the Felix program. Diagonal peak volumes at zero mixing times were estimated by fitting the observed diagonal peaks to an exponential function. For off-diagonal peaks, the intensities of the two symmetries related peaks were averaged prior to normalization. Random numbers were generated by using random function on Microsoft Excel and added for the absent peak data point. Due to the wide range of the spectra, a noisy peak is redefined as having peak intensity less than or equal to 2 times the estimated local volume noise level.

Generation of Static Model Conformers. A combination of two subsets of trial structures totaling 205 conformations was used for the structure analysis. The first subset was generated by annealed dynamics simulation using CERIUS^2 and the Universal force field. The electrostatic term was turned off for all calculations using the Universal force field. Harmonic angle constraints (1000 kcal/(mol Å) for the force constant) between both hydrides and between hydride and phosphorus atoms were applied to prevent the collapse of two ligands on top of one another during dynamics simulation. Simulated annealing at constant volume and constant energy was run for 100 cycles in 10-K increment from 900 to 0 K and from 0 to 900 K with 50 steps at each increment, yielding 100 trial conformations. Each conformation was then mimized without constraints until an rms gradient less that 0.001 kcal/Å was reached. The models generated by simulated annealing differ primarily in the orientation of the bridging phenylene ring relative to the coordination plane defined by the two phosphorus atoms and the Ir. The type of the conformation is defined by the torsion angle C7−P1−Ir1−P2 (torsion 1) and the torsion angle C12−P2−Ir1−P1 (torsion 2). The conformation with the torsion 1 and 2 ranging from −10° to 10° is hereafter called the "planar" conformation. When the phenyl ring moves up to the same side as the axial hydride with torsion 1 less than −10° and torsion 2 greater than 10°, the model is hereafter called the "up" conformation; when the phenyl ring moves down to the opposite side with the torsion 1 greater than 10° and the torsion 2 less than 10°, the model is hereafter called the "down" conformation. The first subset of conformers comprises 30 "up" structures, 10 "planar" structures, and 60 "down" structures.

The second subset of conformers was generated by applying constraints on torsions 1 and 2 during simulated annealing to provide a fuller range of conformers. Harmonic torsion constraints ranged from −50° to 50° in 5° increments with a 1000 kcal/(mol Å) force constant. Angle constraints for both hydrides were used to prevent ligand collapse. Five annealing cycles at constant volume and constant energy were then used for each torsion constraint. The annealing cycles involved cooling from 900 to 600 K followed by heating to 900 K with 10-K increment and 50 steps at each increment. Each annealed structure was then minimized, and its energy was computed with all torsion constraints turned off. The complete set of static conformers was generated by combining 100 structures from the first subset and 105 structures from the second subset. The correlation between the torsion angle (torsion 2) and energy for all conformers used in the trial set is shown in Figure 6. The lowest energy "up" conformation is approximately 4 kcal/mol higher than the lowest energy "down" conformation.

Conformer Population Analysis of the Static Ensemble. Conformer population analysis proceeds by computing the full NOE time course for each conformer in the trial set and then finding the most parsimonious set of conformers that best reproduce the observed data.

(40) Piantini, U.; Sørensen, O. W.; Ernst, R. R. *J. Am. Chem. Soc.* **1982**, *104*, 6800.
(41) Rance, M.; Sørensen, O. W.; Bodenhausen, G.; Wagner, G.; Ernst, R. R.; Wüthrich, K. *Biochem. Biophys. Res. Commun.* **1983**, *117*, 479.
(42) States, D. J.; Haberkorn, R. A.; Ruben, D. J. *J. Magn. Reson.* **1982**, *48*, 286.
(43) Macura, S.; Ernst, R. R. *Mol. Phys.* **1980**, *41*, 95.
(44) Bax, A.; Griffey, R. H.; Hawkins, B. L. *J. Magn. Reson.* **1983**, *55*, 301.
(45) Kessler, H.; Gehrke, M.; Griesinger, C. *Angew. Chem., Int. Ed. Engl.* **1988**, *27*, 490.

Known distances between pairs of protons (21A−21B, 25A−25B, 26A−26B for τ_1 optimization; 1−5, 4−6, 16−17, 13−18 for τ_2 optimization) were used for calibration of the relaxation parameters. The resulting parameters ($\tau_1 = 0.560$ ns; $\tau_2 = 167$ ps) were used for running 2DCPA. The static ensemble was exhaustively fitted with each possible single, double, and triple conformer solution in the fast-exchange mode. Significance testing was done using Hamilton's *F*-test on every possible combination of the 10 best fits of the singles, doubles, and triples.

The populations obtained by 2DCPA depend on the relative weightings of the NOE data. In particular, the extent to which reproduction of absent NOE peaks is included in the data analysis dramatically affects the absolute value of the *R*-factor (and may influence relative conformer populations). Although the dihydride complex **10^{maj}** has 34 inequivalent protons, 458 data points of 595 total points are assigned as absent peaks. The experimental intensities of absent cross-peaks in our analysis were represented as intensities that range from zero to the estimated integration noise level. The contribution of noisy and absent peaks to the error function was given by $(I^{calc} - I^{obs})^2/10$. For all other peaks, the contribution to the error function was $(I^{calc} - I^{obs})^2/(I^{obs})^2$.

A distinctive feature of the 2DCPA is that multiple conformations may be used to fit the NOE data. The inclusion of more than one conformation in NOE analysis always leads to better agreement between computed and observed data. Application of the *F*-test to the calculation will determine whether it is significant to use more than one conformation or even two. The single-conformer fitting shows the lowest *R*-factor ($R = 0.856$) with the "planar" conformation, while the two-conformer fitting leads to a slight decrease of the *R*-factor ($R = 0.830$) with fractional populations of 0.79 and 0.21 of the "planar" and the "up" conformations, respectively. The best fitting of three conformers yields an *R*-factor of 0.828 and corresponds to population of the "planar" conformer and two similar "up" conformers with fractional populations of 0.77, 0.19, and 0.04, respectively. Application of the *F*-test at the 95% confidence level excluding the absent peak data points indicates that it is statistically significant to use two rather than one conformation in fitting the data but that three conformations do not lead to a significantly better fit relative to two conformations.

Kinetics Measurements of Diastereomer Interconversion and Isotope Exchange. NMR kinetics experiments were conducted on a 500-MHz Bruker NMR at −45 or −80 °C. We estimate that the error in NMR-derived rate constants for all experiments is approximately 20%. The data are summarized in Table 6. The diastereomer interconversion is an approach to equilibrium; thus, the measured rate constants are the sum of the forward and reverse reactions.

A 27 mM solution of [IrH_2(COD)((*R*,*R*)-Me-DuPHOS)]BF_4 was formed at −80 °C, and the solution was degassed with cold N_2 for 10 min. The NMR tube was placed in a NMR probe cooled to −45 °C, and the disappearance of the **10^{maj}** dihydrides was followed by ^{1}H NMR. The above kinetics run was repeated for a 55 mM solution of [IrH_2(COD)((*R*,*R*)-Me-DuPHOS)]BF_4 in CD_2Cl_2 and for a 35 mM solution of **10** in acetone-d_6. All three kinetics experiments followed first-order kinetics for a reaction approaching equilibrium. Plots of the $\ln([\mathbf{10^{maj}}]_t - [\mathbf{10^{maj}}]_\infty)$ vs time were found to be linear. The half-lives of the interconversions were 47 ± 10, 47 ± 10, and 64 ± 12 min (these results are indistinguishable within the error of the experiments).

A 55 mM solution of [IrD_2((*R*,*R*)-Me-DuPHOS)(COD)]BF_4 was prepared by bubbling cold D_2 through a solution of [Ir((*R*,*R*)-Me-DuPHOS)(COD)]BF_4 to yield an approximately 50:1 mixture of d_2-**10^{maj}** to d_2-**10^{min}** at −80 °C. The solution was warmed at −45 °C (acetonitrile/N_2 bath) for 5-min intervals under a stream of cold H_2. The ^{1}H and ^{31}P NMRs of the sample were taken at −80 °C. The disappearance of the **10^{maj}**/d_2-**10^{maj}** was followed by ^{31}P NMR. In addition, the appearance of the dihydride resonances for **10^{maj}**/**10^{min}** was monitored via ^{1}H NMR. These experiments were repeated on a 27 mM solution of [IrD_2((*R*,*R*)-Me-DuPHOS)(COD)]BF_4 using 1 atm 8.3% H_2 (balance N_2). As above, the rates for diastereomer interconversion were determined by plotting $\ln([\mathbf{10^{maj}}]_t - [\mathbf{10^{maj}}]_\infty)$ vs time, giving $t_{1/2} = 43 \pm 10$ and 62 ± 12 min, respectively. Rates for isotope exchange were determined by plotting the $\ln([\mathbf{10^{maj}}]_\infty - [\mathbf{10^{maj}}]_t)$ vs time. This reaction was found to follow first-order kinetics, and $t_{1/2} = 47 \pm 10$ and 51 ± 10 min, respectively.

A 27 mM solution of [IrD_2((*R*,*R*)-Me-DuPHOS)(COD)]BF_4 was prepared at −80 °C as before and was purged with cold N_2 for 10 min. The appearance of hydride signals was followed by ^{1}H NMR at −45 °C. The rate for isotope exchange was determined by plotting the $\ln([\mathbf{10^{maj}}]_\infty - [\mathbf{10^{maj}}]_t)$ vs time. This reaction was found to follow first-order kinetics, and the $t_{1/2}$ was 52 ± 10 min. The same experiment was repeated with a 35 mM solution of [IrD_2((*R*,*R*)-Me-DuPHOS)(COD)]BF_4 in acetone. A similar half-life was found (55 ± 11 min).

Deuterium Incorporation into C−H Bonds of 10^{maj}. A 52 mM solution of [IrD_2((*R*,*R*)-Me-DuPHOS)(COD)]BF_4 was prepared in CH_2Cl_2. This solution was purged with N_2 at −80 °C. The sample tube was placed into a NMR probe cooled to −45 °C, and new peaks were observed growing in the ^{2}H NMR at δ 2.5 and 2.8 ppm. These broad peaks were overlapped, and the upfield peak appeared as a shoulder on the peak at δ 2.5 ppm. The peaks appeared to be growing in at similar rates. The rate for isotope exchange was determined by plotting the $\ln([\mathbf{C-D}]_\infty - [\mathbf{C-D}]_t)$ vs time. The integrations of the C−D and M−D sites approached 50% occupancy at equilibrium. This reaction was found to follow first-order kinetics, and the $t_{1/2}$ was 56 ± 12 min. Reactions performed in acetone-d_6 gave similar results.

Due to overlap in the ^{1}H NMR, ^{13}C NMR was used to assign the sites of deuterium incorporation. A 50 mM solution of [IrD_2((*R*,*R*)-Me-DuPHOS)(COD)]BF_4 was prepared in CD_2Cl_2 as above. ^{13}C NMR and DEPT were taken at −80 °C. The solution was warmed for 3 h at −45 °C in an acetonitrile/N_2 bath. ^{13}C NMR and 135 DEPT were taken at −80 °C. The ^{13}C NMR differed from the initial spectrum in two main points: (1) the minor diastereomer **10^{min}** had grown in and (2) two peaks at δ 35.76 (d, $J_{P-H} = 41$ Hz) and 37.89 (s) ppm, corresponding to C1 and C25A, had significantly decreased in size while broadening due to additional coupling (Figure 2.11). This clearly indicated that D was being incorporated at two sites in the molecule. These were found to correspond to positions H1 and H25A. Additional warming did not substantially change the ^{13}C NMR of the sample. Assignment of the proton sites involved in the exchange was determined using HMQC data in combination with previous assignments.

Acknowledgment. Support for this work was provided by the Department of Energy. We thank Dr. Randy Hayashi for solving the crystallograpic structure of [Ir(*R*,*R* Me-DuPhos)(COD)](BF$_4$) and Dr. Monty Wright for assistance with the 2DCPA analysis of the solution NOE data. We gratefully acknowledge helpful discussions with Prof. Chuck Casey and Dr. Charlie Fry.

Supporting Information Available: X-ray crystallographic data for [Ir((*R*,*R*)-Me-DuPhos)(COD)](BF$_4$), ^{1}H NMR spectra for [Ir(bisphosphine)(COD)](BF$_4$) and [IrH_2(bisphosphine)(COD)](BF$_4$) complexes, and NOESY data and 2DCPA analysis for [IrH_2((*R*,*R*)-Me-DuPhos)(COD)](BF$_4$) (126 pages, print/PDF). See any current masthead page for ordering information and Web access instructions.

JA981536B